



GW Ori: Interactions between a Triple-star System and Its Circumtriple Disk in Action

Jiaqing Bi¹, Nienke van der Marel^{1,2}, Ruobing Dong (董若冰)¹, Takayuki Muto³, Rebecca G. Martin⁴, Jeremy L. Smallwood⁴, Jun Hashimoto⁵, Haiyu Baobab Liu⁶, Hideko Nomura^{7,8}, Yasuhiro Hasegawa⁹, Michihiro Takami⁶, Mihoko Konishi¹⁰, Munetake Momose¹¹, Kazuhiro D. Kanagawa¹², Akimasa Kataoka⁷, Tomohiro Ono^{13,14}, Michael L. Sitko^{15,16}, Sanemichi Z. Takahashi^{7,17}, Kengo Tomida^{14,18}, and Takashi Tsukagoshi⁷

¹Department of Physics & Astronomy, University of Victoria, Victoria, BC V8P 5C2, Canada; jiaqing.bi@gmail.com, rbdong@uvic.ca

²Herzberg Astronomy & Astrophysics Programs, National Research Council of Canada, 5071 West Saanich Road, Victoria, BC V9E 2E7, Canada

³Division of Liberal Arts, Kogakuin University, 1-24-2 Nishi-Shinjuku, Shinjuku-ku, Tokyo 163-8677, Japan

⁴Department of Physics & Astronomy, University of Nevada, Las Vegas, 4505 South Maryland Parkway, Las Vegas, NV 89154, USA

⁵Astrobiology Center, National Institutes of Natural Sciences, 2-21-1 Osawa, Mitaka, Tokyo 181-8588, Japan

⁶Academia Sinica Institute of Astronomy & Astrophysics, No. 1, Section 4, Roosevelt Road, Taipei 10617, Taiwan

⁷Division of Science, National Astronomical Observatory of Japan, 2-21-1 Osawa, Mitaka, Tokyo 181-8588, Japan

⁸Department of Earth & Planetary Sciences, Tokyo Institute of Technology, 2-12-1 Ookayama, Meguro, Tokyo 152-8551, Japan

⁹Jet Propulsion Laboratory, California Institute of Technology, Pasadena, CA 91109, USA

¹⁰Faculty of Science & Technology, Oita University, 700 Dannoharu, Oita 870-1192, Japan

¹¹College of Science, Ibaraki University, 2-1-1 Bunkyo, Mito, Ibaraki 310-8512, Japan

¹²Research Center for the Early Universe, Graduate School of Science, University of Tokyo, Bunkyo, Tokyo 113-0033, Japan

¹³Department of Astrophysical Sciences, Princeton University, Princeton, NJ 08544, USA

¹⁴Department of Earth & Space Science, Osaka University, Toyonaka, Osaka 560-0043, Japan

¹⁵Department of Physics, University of Cincinnati, Cincinnati, OH 45221, USA

¹⁶Space Science Institute, 475 Walnut Street, Suite 205, Boulder, CO 80301, USA

¹⁷Department of Applied Physics, Kogakuin University, 1-24-2 Nishi-Shinjuku, Shinjuku-ku, Tokyo 163-8677, Japan

¹⁸Astronomical Institute, Tohoku University, Sendai, Miyagi 980-8578, Japan

Received 2020 March 28; revised 2020 April 26; accepted 2020 April 29; published 2020 May 21

Abstract

GW Ori is a hierarchical triple system with a rare circumtriple disk. We present Atacama Large Millimeter/submillimeter Array (ALMA) observations of 1.3 mm dust continuum and $^{12}\text{CO } J = 2 - 1$ molecular gas emission of the disk. For the first time, we identify three dust rings in the GW Ori disk at ~ 46 , 188, and 338 au, with estimated dust mass of 74, 168, and 245 Earth masses, respectively. To our knowledge, its outermost ring is the largest dust ring ever found in protoplanetary disks. We use visibility modeling of dust continuum to show that the disk has misaligned parts, and the innermost dust ring is eccentric. The disk misalignment is also suggested by the CO kinematics. We interpret these substructures as evidence of ongoing dynamical interactions between the triple stars and the circumtriple disk.

Unified Astronomy Thesaurus concepts: [Protoplanetary disks \(1300\)](#); [Planet formation \(1241\)](#); [Circumstellar matter \(241\)](#); [Pre-main sequence stars \(1290\)](#)

Supporting material: data behind figure

1. Introduction

GW Ori is a hierarchical triple system (Berger et al. 2011) at a distance of 402 ± 10 parsecs (Gaia Collaboration et al. 2018). Two of the stars (GW Ori AB) compose a spectroscopic binary with a separation of ~ 1 au (Mathieu et al. 1991). A tertiary component (GW Ori C) was detected by near-infrared interferometry at a projected distance of ~ 8 au (Berger et al. 2011). The stellar masses have been constrained to be ~ 2.7 , 1.7, and $0.9 M_{\odot}$, respectively (Czekala et al. 2017). The system harbors a rare circumtriple disk, with dust extending to ~ 400 au, and gas extending to ~ 1300 au (Fang et al. 2017). Spectral energy distribution (SED) modeling indicates a gap in the disk at 25–55 au (Fang et al. 2014).

Here we present high resolution ALMA observations in the disk around GW Ori at 1.3 mm dust continuum emission and $^{12}\text{CO } J = 2 - 1$ emission, where we find new substructures of the disk that indicate ongoing disk–star interactions. We arrange the paper as follows: In Section 2, we describe the

setups of the ALMA observations and data reduction. In Section 3, we present the imaged results of dust continuum and $^{12}\text{CO } J = 2 - 1$ observations. In Section 4, we present results of dust continuum visibility modeling. In Section 5, we discuss the possible origins of the observed substructures. In Section 6, we summarize our findings and raise some open questions.

2. Observation and Data Reduction

The observations were taken on 2017 December 10 (ID: 2017.1.00286.S). The disk was observed in Band 6 (1.3 mm) by 46 antennas, with baseline lengths ranging from 15 to 3321 m. The total on source integration time was 1.6 hours. There were two 1.875 GHz-wide basebands centered at 217 and 233 GHz for continuum emission, and three basebands with 117 MHz bandwidths and 112 kHz resolution, centered at 230.518, 219.541, and 220.380 GHz to cover the ^{12}CO , ^{13}CO , and $\text{C}^{18}\text{O } J = 2 - 1$ lines.

The data were calibrated by the pipeline calibration script provided by ALMA. We used the Common Astronomy Software Applications package (CASA; version 5.1.1–5; McMullin et al. 2007) to process the data. We adopted CASA task CLEAN to image the continuum map (Figure 1(a)), with the UNIFORM weighting scheme and a $0''.098$ circular restoring

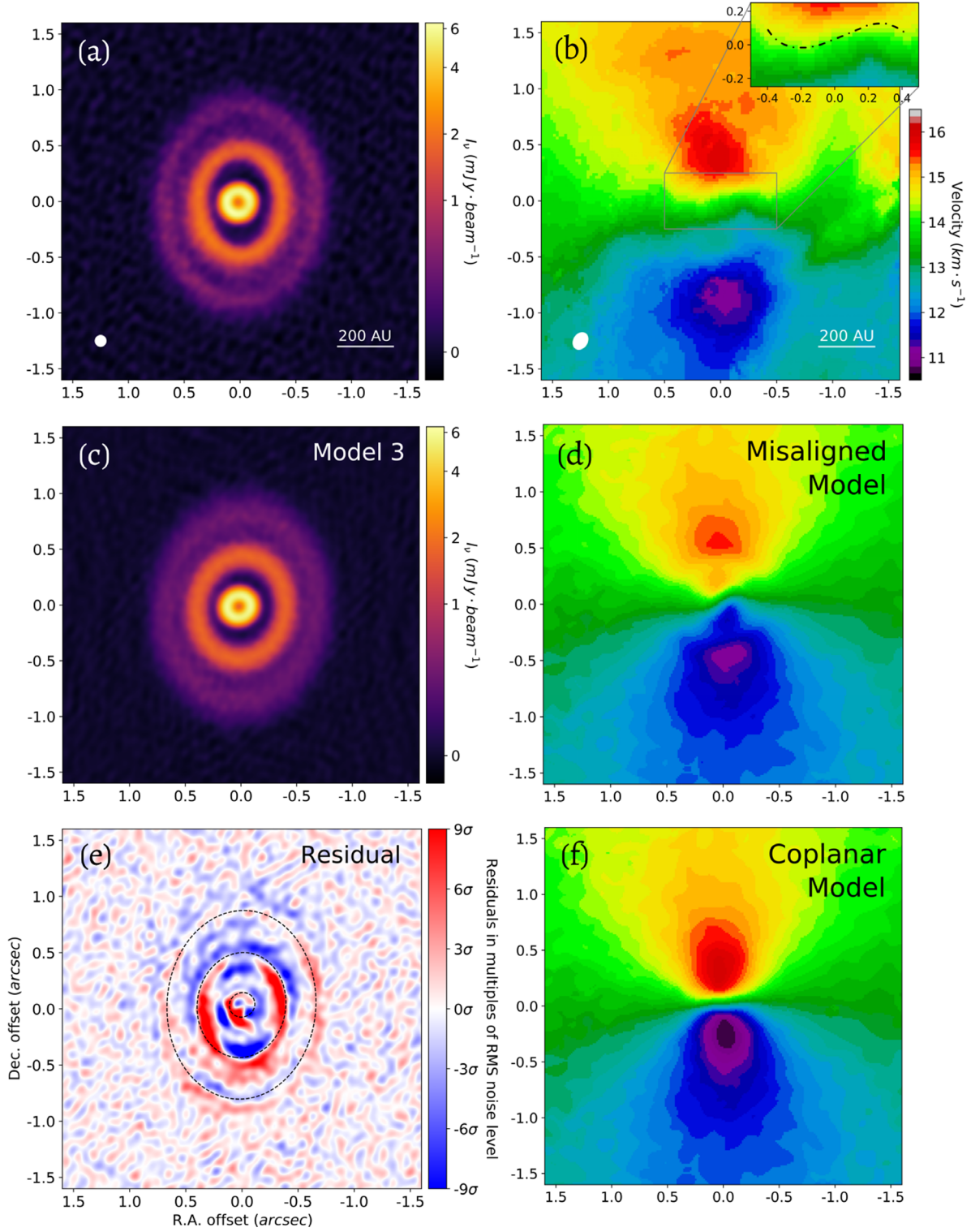


Figure 1. All panels are centered on the stellar position provided by GAIA DR2 (ICRS R.A. = $5^{\text{h}}29^{\text{m}}08^{\text{s}}.390$ and decl. = $11^{\circ}52'12''.661$). (a) The ALMA self-calibrated dust continuum map performed with a $0''.098$ circular beam (bottom left corner; rms noise level $\sigma \sim 40 \mu\text{Jy beam}^{-1}$). A larger view of this panel is provided in Appendix B. (b) The ALMA $^{12}\text{CO } J = 2-1$ first-moment map performed with a $0''.122 \times 0''.159$ beam with a position angle of -32.3 (bottom left corner). The inset shows a $1''$ by $0''.5$ wide (40 by 20 au) zoom, and the dotted-dashed line highlights the shape of the twist. The averaged uncertainty in the inset region is $\sim 0.2 \text{ km s}^{-1}$. (c) Simulated ALMA continuum emission map of Model 3, produced in the same way as panel (a). (d) The synthetic first-moment map of the misaligned disk model, applying the model parameters listed in Table 2. The color scheme is the same as that in panel (b). (e) The residual map of Model 3. Dashed ellipses mark the fitted location of the three dust rings. The colorbar shows the residual magnitude in units of rms noise level ($1\sigma = \sim 40 \mu\text{Jy beam}^{-1} = \sim 0.6\%$ of peak surface density). (f) The synthetic first-moment map of the coplanar disk model, with an inclination of 37.9 and a position angle of -5° throughout the disk. The color scheme is the same as that in panel (b). The data behind panels (a) and (b) are available in the .tar.gz package in two FITS files.

(The data used to create this figure are available.)

beam. We performed phase self-calibration onto the image with a solution interval of 20 s. This resulted in an rms noise level of $\sim 40 \mu\text{Jy beam}^{-1}$ and an enhanced peak signal-to-noise ratio (SNR) of ~ 157 , compared with $\sim 63 \mu\text{Jy beam}^{-1}$ and ~ 90 before self-calibration, respectively. The integrated flux density of the disk ($195 \pm 20 \text{ mJy}$) is consistent with the result from previous ALMA observations ($202 \pm 20 \text{ mJy}$; Czekala et al. 2017).

The $^{12}\text{CO } J = 2 - 1$ line data were obtained (after subtracting the continuum on the self-calibrated data) in the BRIGGS weighting scheme with robust = 0.5, and velocity resolution 0.5 km s^{-1} . The resulting line cube has a beam size of $0''.122 \times 0''.159$ at the position angle $-32^\circ.3$. The noise level is $\sim 1.4 \text{ mJy beam}^{-1}$ per channel and the peak signal-to-noise ratio is ~ 83 . Line emission was detected between 7.0 and 20.0 km s^{-1} with a central velocity of 13.5 km s^{-1} . The integrated flux is $60.6 \text{ Jy km s}^{-1}$, assuming a $2''$ radius. The intensity-weighted velocity map (a.k.a., the first-moment map) was constructed by calculating the intensity-weighted velocity with a threshold of three times the noise level. The averaged uncertainty of the twisted pattern in the first-moment map (i.e., the inset in Figure 1(b)) is $\sim 0.2 \text{ km s}^{-1}$, derived from error propagation theory, assuming the uncertainty of velocity due to the channel resolution is 0.25 km s^{-1} . The observations of the CO isotopologues C^{18}O and $^{13}\text{CO } J = 2 - 1$ emission will be presented in future work.

3. Observational Results

3.1. Dust Continuum Emission

Figure 1(a) shows the continuum map with spatial resolution of $0''.098$ ($\sim 39 \text{ au}$). We identify three dust rings with different apparent shapes in the disk at ~ 46 , 188 , and 338 au (hereafter the inner, middle, and outer ring). The location of the inner ring coincides with the predicted cavity size from SED modeling (Fang et al. 2017). The continuum flux densities of the inner, middle, and outer ring are 42 ± 4 , 95 ± 10 , and $58 \pm 6 \text{ mJy}$, respectively. To our knowledge, the outer ring is the largest ever found in protoplanetary disks.

The three rings harbor an enormous amount of solid material. We estimate the dust (solid) mass M_{dust} of the rings with the equation provided in Hildebrand (1983)

$$M_{\text{dust}} = \frac{F_\nu d^2}{B_\nu(T_{\text{dust}}) \kappa_\nu}, \quad (1)$$

where F_ν is the continuum surface brightness at a submillimeter frequency ν , d is the distance from the observer to the source, $B_\nu(T_{\text{dust}})$ is the Planck function at the dust temperature T_{dust} , and κ_ν is the dust opacity. The dust temperature is estimated using a fitting function provided by Dong et al. (2018b)

$$T_{\text{dust}} = 30 \left(\frac{L_\star}{38 L_\odot} \right)^{1/4} \left(\frac{r}{100 \text{ AU}} \right)^{-1/2}, \quad (2)$$

where L_\star is the total stellar luminosity, and r is the location of the ring. The stellar luminosity modified by the distance provided by GAIA DR2 is $49.3 \pm 7.4 L_\odot$ (Calvet et al. 2004; Gaia Collaboration et al. 2018). We assume a dust grain opacity of $10 \text{ cm}^2 \text{ g}^{-1}$ at 1000 GHz with a power-law index of 1 (Beckwith et al. 1990). We estimate the dust masses of the rings to be 74 ± 8 , 168 ± 19 , and $245 \pm 28 M_\oplus$, respectively, with the uncertainties incorporating the uncertainties in the

surface brightness of the rings, source distance, stellar luminosity, and radial location of the rings.

3.2. $^{12}\text{CO } J = 2 - 1$ Emission

Figure 1(b) shows the first-moment map of $^{12}\text{CO } J = 2 - 1$ emission (with the zeroth-moment map provided in Appendix A). For regular Keplerian rotating disks, we expect a well-defined butterfly-like pattern in the first-moment map. However, we find a twisted pattern inside $\sim 0''.2$, which may result from a misalignment between the inner and outer parts of the disk (i.e., having different inclinations and orientations; Rosenfeld et al. 2014), as has been found in the disks around, e.g., HD 142527 (Casassus et al. 2015; Marino et al. 2015) and HD 143006 (Benisty et al. 2018; Pérez et al. 2018).

4. Modeling of Dust and Gas Emission

The different apparent shapes of the rings could result from a few scenarios, such as coplanar rings with different eccentricities, circular rings with different inclinations, or rings with both different eccentricities and inclinations. Here we present evidence for disk misalignment and disk eccentricity found in modeling the dust and gas emission.

4.1. Visibility Modeling of the Dust Continuum Emission

We fit the dust continuum map assuming that there are three dust rings in the disk with Gaussian radial profiles of surface brightness

$$F_i(r) = F_{0,i} e^{-\frac{(r-r_i)^2}{2\sigma_i^2}}, \quad (3)$$

where F_i is the surface brightness as a function of the distance to the center r , with $i = 1, 2, 3$ denoting parameters for the inner, middle, and outer ring, respectively. $F_{0,i}$ is the peak surface brightness, r_i is the radius of the ring (i.e., where the ring has the highest surface brightness), and σ_i is the standard deviation.

Initially, we assume all three rings are intrinsically circular when viewed face-on, and their different apparent shapes entirely originate from different inclinations. For each ring, we assume an independent set of peak surface brightness, center location, radius, width, inclination, and position angle as the model parameters. We call this combination of assumptions Model 1.

After projecting the rings according to their position angles and inclinations, we calculate the synthetic visibility of the models using GALARIO (Tazzari et al. 2018), and launch MCMC parameter surveys to derive posterior distribution of model parameters using EMCEE (Foreman-Mackey et al. 2013). In the MCMC parameter surveys, the likelihood function L is defined as

$$\ln L = -\frac{1}{2} \sum_{j=1}^N m_j \times [(ReV_{\text{obs},j} - ReV_{\text{mod},j})^2 + (ImV_{\text{obs},j} - ImV_{\text{mod},j})^2], \quad (4)$$

where V_{obs} is the visibility data from ALMA observations, V_{mod} is the synthetic model visibility, N is the total number of visibility data points in V_{obs} , and m_j is the weight of each visibility data point in V_{obs} . The prior function is set to guarantee the surface brightness, ring radius, and ring width do not go below zero, the position angle does not go beyond $(-90, 90)$ degrees, and the inclination does not go beyond $(0, 90)$ degrees. For each model, there are 144 chains spread in

Table 1
The Complete MCMC Result of Dust Continuum Visibility Modeling

(a) Model 1			
	Inner Ring	Middle Ring	Outer Ring
R.A Offset [arcsecond]	$1.89 \times 10^{-2} +9.47 \times 10^{-5}$ -9.49×10^{-5}	$-2.44 \times 10^{-3} +1.82 \times 10^{-4}$ -2.08×10^{-4}	$-4.24 \times 10^{-3} +4.64 \times 10^{-4}$ -3.91×10^{-4}
decl. Offset [arcsecond]	$-1.32 \times 10^{-2} +1.09 \times 10^{-4}$ -1.01×10^{-4}	$-2.26 \times 10^{-2} +2.22 \times 10^{-4}$ -2.06×10^{-4}	$-1.21 \times 10^{-2} +6.57 \times 10^{-4}$ -4.67×10^{-4}
Ring Radius [arcsecond]	$1.15 \times 10^{-1} +1.46 \times 10^{-4}$ -1.48×10^{-4}	$4.68 \times 10^{-1} +3.07 \times 10^{-4}$ -2.92×10^{-4}	$8.40 \times 10^{-1} +1.03 \times 10^{-3}$ -1.15×10^{-3}
Ring Width [arcsecond]	$4.97 \times 10^{-2} +3.16 \times 10^{-4}$ -6.24×10^{-4}	$1.74 \times 10^{-1} +6.69 \times 10^{-4}$ -7.56×10^{-4}	$3.32 \times 10^{-1} +1.84 \times 10^{-3}$ -2.78×10^{-3}
Surface Brightness [Jy/pixel]	$2.49 \times 10^{-4} +1.80 \times 10^{-6}$ -1.56×10^{-6}	$3.96 \times 10^{-5} +8.67 \times 10^{-8}$ -1.69×10^{-7}	$1.13 \times 10^{-5} +2.77 \times 10^{-8}$ -5.52×10^{-7}
Inclination [degree]	$22.24 +0.23$ -0.31	$32.62 +0.07$ -0.11	$37.93 +0.09$ -0.08
Position Angle [degree]	$-60.75 +1.06$ -0.56	$-7.43 +0.19$ -0.12	$-3.57 +0.15$ -0.12
(b) Model 2			
	Inner Ring	Middle Ring	Outer Ring
R.A Offset [arcsecond]		$1.77 \times 10^{-2} +1.69 \times 10^{-4}$ -1.61×10^{-4}	
decl. Offset [arcsecond]		$-2.22 \times 10^{-2} +1.95 \times 10^{-4}$ -1.99×10^{-4}	
Ring Radius [arcsecond]	$1.17 \times 10^{-1} +1.36 \times 10^{-4}$ -1.35×10^{-4}	$4.68 \times 10^{-1} +2.88 \times 10^{-4}$ -2.71×10^{-4}	$8.40 \times 10^{-1} +9.48 \times 10^{-4}$ -9.53×10^{-4}
Ring Width [arcsecond]	$4.97 \times 10^{-2} +3.16 \times 10^{-4}$ -3.91×10^{-4}	$1.74 \times 10^{-1} +6.66 \times 10^{-4}$ -6.03×10^{-4}	$3.30 \times 10^{-1} +1.68 \times 10^{-3}$ -1.96×10^{-3}
Surface Brightness [Jy/pixel]	$2.51 \times 10^{-4} +1.53 \times 10^{-6}$ -1.55×10^{-6}	$3.96 \times 10^{-5} +8.20 \times 10^{-8}$ -1.01×10^{-7}	$1.13 \times 10^{-5} +2.65 \times 10^{-8}$ -3.37×10^{-8}
Inclination [degree]	$23.15 +0.22$ -0.23	$32.64 +0.07$ -0.07	$37.91 +0.08$ -0.07
Position Angle [degree]	$-55.67 +0.61$ -0.50	$-7.44 +0.14$ -0.12	$-3.60 +0.13$ -0.11
Apoapsis Angle [degree]	$65.04 +0.50$ -0.49
Eccentricity	$0.21 +1.75 \times 10^{-3}$ -1.43×10^{-3}
(c) Model 3			
	Inner Ring	Middle Ring	Outer Ring
Ring Radius [arcsecond]	$1.16 \times 10^{-1} +1.20 \times 10^{-4}$ -1.49×10^{-4}	$4.68 \times 10^{-1} +2.72 \times 10^{-4}$ -2.98×10^{-4}	$8.37 \times 10^{-1} +8.95 \times 10^{-4}$ -1.06×10^{-3}
Ring Width [arcsecond]	$4.99 \times 10^{-2} +3.06 \times 10^{-4}$ -3.86×10^{-4}	$1.73 \times 10^{-1} +6.33 \times 10^{-4}$ -5.98×10^{-4}	$3.39 \times 10^{-1} +1.90 \times 10^{-3}$ -1.85×10^{-3}
Surface Brightness [Jy/pixel]	$2.47 \times 10^{-4} +1.64 \times 10^{-6}$ -1.42×10^{-6}	$3.94 \times 10^{-5} +8.55 \times 10^{-8}$ -1.12×10^{-7}	$1.13 \times 10^{-5} +2.63 \times 10^{-8}$ -3.33×10^{-8}
Inclination [degree]	$20.63 +0.23$ -0.29	$32.86 +0.06$ -0.07	$37.96 +0.09$ -0.08
Position Angle [degree]	$-60.37 +0.81$ -0.65	$-7.26 +0.13$ -0.13	$-3.49 +0.13$ -0.12
Apoapsis Angle [degree]	$121.39 +0.26$ -0.25
Eccentricity	$0.19 +8.55 \times 10^{-4}$ -6.46×10^{-4}

Note. The radius of each ring is the location of the peak in our model in Section 4, and the width is the full width at half maximum (FWHM) of the profile. The center offsets for Model 1 and Model 2 are relative to the center in Model 3, which is the location of GW Ori provided by GAIA DR2 (ICRS R.A. = $5^{\text{h}}29^{\text{m}}08^{\text{s}}.390$ and decl. = $11^{\circ}52'12''.661$). The position angles and apoapsis angles are measured east of north. The inclination is defined in the range from 0° to 90° , with 0° denoting face-on. The pixel size in the unit of surface brightness is determined internally by GALARIO.

the hyperspace of parameters. Each chain has 15,000 iterations including 10,000 burn-in iterations. The results of the parameter surveys are listed in Table 1.

The fitting result of Model 1, listed in Table 1(a), suggests that the three rings have statistically different centers. Particularly, the center of the inner ring differs from the centers of the outer two by $\sim 20\%$ of the inner ring's radius. This nonconcentricity indicates nonzero intrinsic eccentricities in the rings, particularly the inner ring (see Section 5.1).

We explore the nonzero intrinsic eccentricity in the inner ring with two models. In both models, the outer two rings are intrinsically circular and concentric. Their center coincides with one of the two foci of the inner ring. In Model 2, that center is set free, while in Model 3 it is assumed to coincide with the stellar position provided by GAIA DR2 (Gaia Collaboration et al. 2018). In those two models, we introduce two more

parameters for the intrinsic eccentricity and apoapsis angle of the inner ring. The position angle only indicates the direction to the ascending node on the axis along which the ring is inclined. The fitting results are listed in Tables 1(b) and (c), and the following calculations are based on the result of Model 3.

Figures 1(c) and (e) show the model image and the residual map of Model 3, respectively. The residual map is produced by subtracting model from data in the visibility plane, and then imaging the results in the same way used for the observations. We interpret the residuals as additional substructures on top of the ideal model (e.g., a warp within the ring; Huang et al. 2020).

All three models yield roughly consistent inclinations and position angles of each ring. However, we cannot determine the mutual inclinations between them (i.e., the angles between their angular momentum vectors) from dust emission modeling alone, due to the unknown direction of orbital motion.

Table 2
The Parameters Used in the Gas Kinematics Modeling

Inner Ring	Outer Ring	Longitude of the Ascending Node	Inclination
(au)	(au)	(degree)	(degree)
0	32	No Emission	
32	48	-60	22.3
48	153	-10	17.3
153	1000	-5	37.9

Note. The annuli are concentric with the center located at the stellar position provided by GAIA DR2 (ICRS R.A. = $5^{\text{h}}29^{\text{m}}08^{\text{s}}.390$ and decl. = $11^{\circ}52'12''661$). The longitude of the ascending node is measured east of north, and the inclination is defined in the range from 0° to 90° with 0° meaning face-on. The disk model is composed of an empty inner cavity and three annuli, inside out. The inner annulus (from 32 to 48 au) is for the inner dust ring. The outer annulus (from 153 to 1000 au) is for the middle and outer dust rings. The middle annulus (from 48 to 153 au) is for the gap in between.

4.2. Kinematics Modeling of the $^{12}\text{CO } J = 2 - 1$ Emission

Following the prescription and parameter values used to fit low resolution CO isotopologue data of GW Ori (Fang et al. 2017), we set up a gas surface density model using a power-law profile with an exponential tail

$$\Sigma(r) = \Sigma_c \left(\frac{r}{r_c} \right)^{-\gamma} e^{[-(r-r_c)^2-\gamma]}, \quad (5)$$

and the aspect ratio h/r parameterized as

$$\frac{h}{r} = \left(\frac{h}{r} \right)_c \left(\frac{r}{r_c} \right)^{\psi}, \quad (6)$$

where Σ_c and $(h/r)_c$ are corresponding values at the characteristic scaling radius r_c . The disk mass is taken as $0.12 M_{\odot}$, corresponding to $\Sigma_c = 3 \text{ g cm}^{-2}$ for $r_c = 320 \text{ au}$, with $\gamma = 1.0$, $(h/r)_c = 0.18$, and $\psi = 0.1$. The dust surface density profile is set by assuming a gas-to-dust ratio of 100, and decreasing the dust surface density by a factor of 1000 inside the derived gap radii: inside 37 au, from 56 to 153 au, and from 221 to 269 au. The ^{12}CO channel maps are then computed and ray-traced by the physical-chemical modeling code DALI (Bruderer 2013), which simultaneously solves the heating-cooling balance of the gas and chemistry to determine the gas temperature, molecular abundances, and molecular excitation for a given density structure.

Similar to Walsh et al. (2017), we model the misaligned disk with an inner cavity and three annuli each with its own inclination and position angle,¹⁹ as listed in Table 2. The channel map is run through the ALMA simulator using the settings of the ALMA observations. The resulting first-moment map is shown in Figure 1(d). In Figure 1(f) we show the simulated first-moment map for another model as a comparison, in which the disk is coplanar with an inclination of 37.9° and a position angle of -5° .

The models show that the $^{12}\text{CO } J = 2 - 1$ first-moment map in the ALMA observation cannot be reproduced by a

¹⁹ DALI is unable to vary inclination as a function of radius. The final channel map is constructed by concatenating three channel maps, each for one component, ray-traced at its inclination and position angle and cut out at the specified radius range listed in Table 2.

coplanar disk. Instead, the misaligned disk model described in Table 2 matches the observed first-moment map better, indicating the presence of misalignment in the GW Ori disk.

5. Discussions

Several disks have been observed to have nonzero eccentricity and/or misalignment (e.g., MWC 758, Dong et al. 2018a; HD 142527, Casassus et al. 2015; Marino et al. 2015; and HD 143006, Benisty et al. 2018; Pérez et al. 2018). Unlike most of them, in which the origin is uncertain, the GW Ori system provides a strong and direct link between substructures and star-disk gravitational interactions. Therefore, it offers a unique laboratory to probe three-dimensional star-disk interactions. In this section, we discuss the possible origins of the observed substructures due to star-disk interactions.

5.1. Disk Eccentricity

The A-B binary and the C component can be dynamically viewed as an AB-C binary. The eccentricity of the circumbinary disk may increase through resonant interactions with the binary (Papaloizou et al. 2001). In the case of no binary-disk misalignment, the binary's perturbing gravitational potential on the midplane of the disk is given by Lubow (1991). The coupling of this perturbing potential with the imposed eccentricity of the disk excites density waves at the 1:3 outer eccentric Lindblad resonance, which lead to angular momentum removal in the inner parts of the disk. As no energy is removed along with the angular momentum in this process, the disk orbit cannot remain circular (Papaloizou et al. 2001). In the case of GW Ori, the inner dust ring is the most susceptible to this effect, which could explain why its center in Model 1 is more deviated from those of the other two rings.

5.2. Binary-disk Misalignment

Our dust and gas observations alone cannot break the degeneracy in the mutual inclination between different parts in the disk due to the unknown on-sky projected orbital direction of the disk. Previous studies indicate that the on-sky projected gas motion is likely to be clockwise (Czekala et al. 2017), same as the orbital motion of GW Ori C given by astrometric observations (Berger et al. 2011). Given the inclination and longitude of ascending node of the AB-C binary orbit being 150 ± 7 and 282 ± 9 degrees (Czekala et al. 2017), we assume that the entire disk has the same clockwise on-sky projected orbital direction. Following Fekel (1981), we find out that the binary-disk misalignments at 46 au (the inner ring), 100 au (a gap), 188 au (the middle ring), and 338 au (outer ring) are 11 ± 6 , ~ 28 ,²⁰ 35 ± 5 , and 40 ± 5 degrees, respectively. A schematic diagram of our disk model is displayed in Figure 2. Therefore, the inner ring and the AB-C binary plane are close to being coplanar, and there is a monotonic trend of binary-disk misalignment from $\sim 10^{\circ}$ at $\sim 50 \text{ au}$ to $\sim 40^{\circ}$ at $\sim 340 \text{ au}$, consistent with the expected outcome of the disk misalignment (see Section 5.3).

Several mechanisms could produce an initial binary-disk misalignment, such as turbulence in the star-forming gas clouds (Bate 2012), binary formation in the gas cloud whose physical

²⁰ The manual fitting of the gas model cannot provide any uncertainties for the gap between the inner and middle rings.

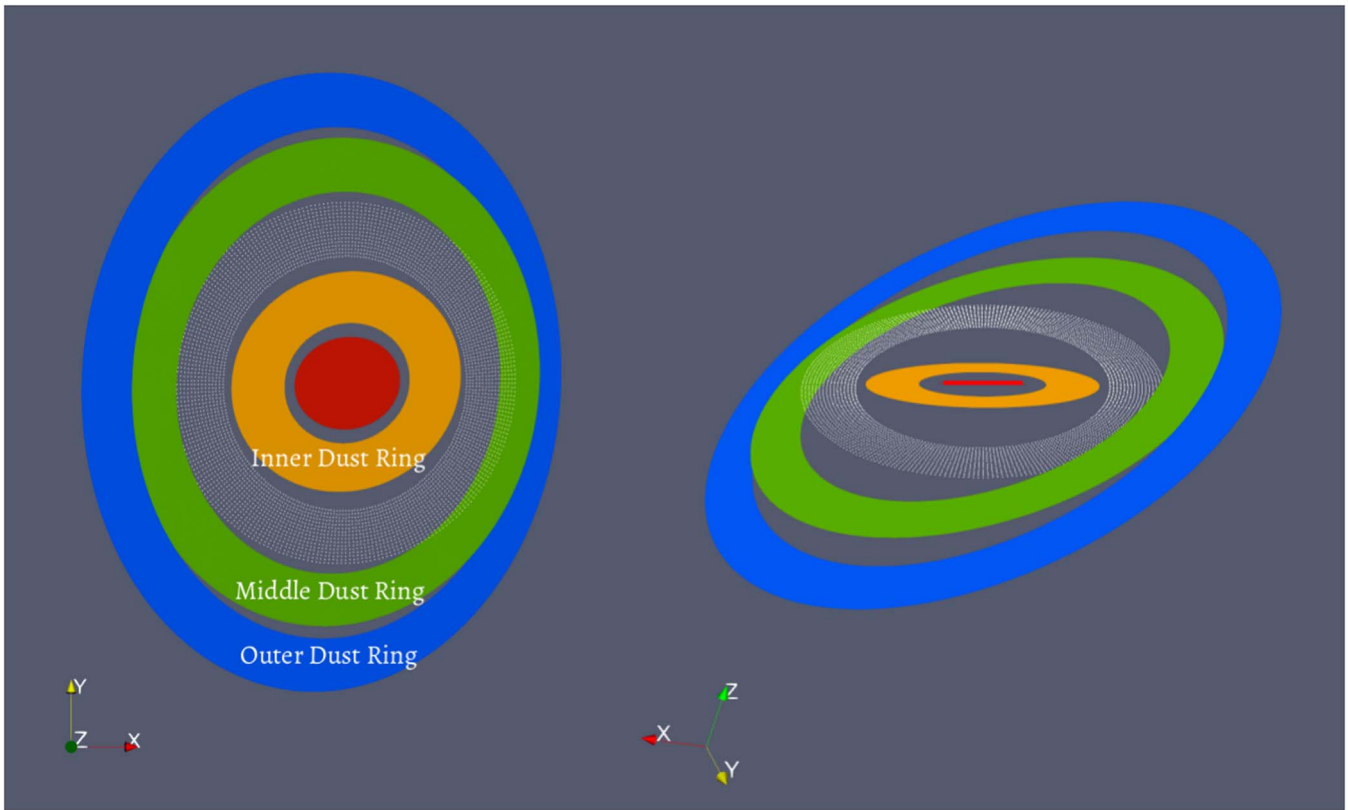


Figure 2. Schematic diagram showing the proposed geometry of the system. Orbital planes of the AB-C binary (red), the inner dust ring (orange), the gap between the inner and middle dust rings (white dots), the middle dust ring (green), and the outer dust ring (blue) are marked inside out. The left panel is a sky-projected view, and in the right panel the binary is edge-on. The size of the disk components are not to-scale. The orientation axes are shown at the bottom left corner of each panel, with the x -axis being antiparallel to the R.A. direction, the y -axis being parallel to the decl. direction, and the z -axis pointing at the observer.

axes are misaligned to the rotation axis (Bonnell & Bastien 1992), and accretion of cloud materials with misaligned angular momentum with respect to the binary after the binary formation (Bate 2018).

5.3. Misalignment within the Disk

A test particle orbiting a binary on a misaligned orbit undergoes nodal precession due to gravitational perturbations from the binary (Nixon et al. 2011; Facchini et al. 2018). For a protoplanetary disk in the bending-wave regime (i.e., where the aspect ratio is higher than the α -prescription of viscosity; Shakura & Sunyaev 1973), disk parts at different radii shall undergo global precession like a rigid body with possibly a small warp (Smallwood et al. 2019). Therefore, the timescale of radial communication of disk materials (i.e., for pressure-induced bending waves propagating at half of the sound speed) and the timescale of global precession determine whether the disk can develop a misalignment inside.

Assuming an inner radius at 32 au (3–4 times the AB-C binary semimajor axis; Czekala et al. 2017; Kraus et al. 2020) and an outer radius at 1300 au (size of the gas disk; Fang et al. 2017), the global precession timescale of the entire disk is ~ 0.83 Myr, and the radial communication timescale is ~ 0.06 Myr (see Appendix D.1 and D.2 for detailed calculations). The radial communication is able to prevent the disk from breaking or developing a significant warp, and we would not expect the observed large deviations in the inclination and position angle between the inner and middle ring. Therefore, we propose that the gap between the inner and middle ring is

deep enough to break the disk into two parts (hereafter the inner and outer disk), undergoing nodal precession independently, due to another mechanism.

Due to the viscous dissipation, the precessing disk is torqued toward either polar alignment (i.e., the binary-disk misalignment becomes 90° ; Martin & Lubow 2017; Zanazzi & Lai 2018), or coplanar alignment/counteralignment. The minimum critical initial binary-disk misalignment for which a disk moves toward polar alignment is $\sim 63^\circ$ in the limit of zero disk mass. Since a higher disk mass will lead to a larger critical angle (Martin & Lubow 2019), the GW Ori disk is most likely moving toward coplanar alignment. As we propose that the disk breaks into two parts undergoing global precession independently, they are also aligning to the binary independently on different timescales.

Assuming the radial communication is blocked at 60 au, we estimate the alignment timescales to be ~ 1 Myr for the inner disk and above 100 Myr for the outer disk (see Appendix D.3). This is consistent with the observed significantly smaller inclination of the inner ring with respect to the binary than those of the outer rings. The latter are likely inherited from birth and have not evolved much given the system age.

If the radial communication is also blocked at the gap between the middle and outer rings (e.g., ~ 250 au), the nodal precession timescales for the middle and outer rings would be ~ 0.6 Myr and ~ 120 Myr, respectively, and the two rings are likely to develop significantly different position angles. Thus we propose that the gap between the middle and outer rings does not cut off the radial communication, and the two rings

precess roughly as a rigid body with only a small warp between them.

5.4. Hydrodynamic Simulations

The analytical results suggest that the radial communication is able to prevent the binary from breaking the disk (e.g., Nixon et al. 2013). As a result, we propose a break at ~ 60 au that is due to other mechanisms in order to explain the observed structures. We carry out a demonstrative smoothed particle hydrodynamic (SPH) simulation with the PHANTOM code (Lodato & Price 2010; Price & Federrath 2010; Price et al. 2018) to test the nonbreaking hypothesis in the nonlinear regime. The results are shown in Figure 3.

We model the triple-star system as the outer binary in order to speed up the simulation. The simulation consists of 10^6 equal mass Lagrangian SPH particles initially distributed from $r_{\text{in}} = 40$ au to $r_{\text{out}} = 400$ au. The initial truncation radius of the disk does not affect the simulation significantly, since the material moves inwards quickly due to the short local viscous timescale. A smaller initial outer truncation radius r_{out} than what is observed is chosen in order to better resolve the disk. The binary begins at apastron with $e_b = 0.22$ and $a_b = 9.2$ au (Czekala et al. 2017). The accretion radius of each binary component is 4 au. Particles within this radius are accreted, and their mass and angular momentum are added to the star. We ignore the effect of self-gravity since it has no effect on the nodal precession rate of flat circumbinary disks.

The initial surface density profile is taken by

$$\Sigma(r) = \Sigma_0(r/r_0)^{-3/2}, \quad (7)$$

where Σ_0 is the density normalization at $r_0 = 40$ au, corresponding to a total disk mass of $0.1 M_\odot$. We take a locally isothermal disk with a constant aspect ratio $h/r = 0.05$, where h is the scale height. The Shakura & Sunyaev (1973) α parameter varies in the range 0.008–0.013 over the disk. The SPH artificial viscosity $\alpha_{\text{AV}} = 0.31$ mimics a disk with

$$\alpha \approx \frac{\alpha_{\text{AV}} \langle H \rangle}{10 h} \quad (8)$$

(Lodato & Price 2010), where $\langle H \rangle$ is the mean smoothing length on particles in a cylindrical ring at a given radius and we take $\beta_{\text{AV}} = 2$. The disk is resolved with average smoothing length per scale height of 0.32.

The evolution of surface density, binary-disk misalignment, and longitude of the ascending node at different radii suggest that the disk does not show any sign of breaking in 3000 binary’s orbital periods (~ 0.04 Myr), which is sufficiently long to tell if the disk would break or not since the radial communication timescale in the simulation is ~ 0.01 Myr. Instead, the disk presents a global warp. The warp is not taken into account in the analytic estimates. The small outer truncation radius in the simulation leads to a faster precession timescale than that predicted by the analytic model, comparable to the radial communication timescale. The simulations suggests that unless the disk is very cool (i.e., low aspect ratio) and in the viscous regime, some other mechanism, e.g., a companion, is needed to break the disk at the gap between the inner and middle rings. This mechanism may also be responsible for producing the observed misalignment in the disk.

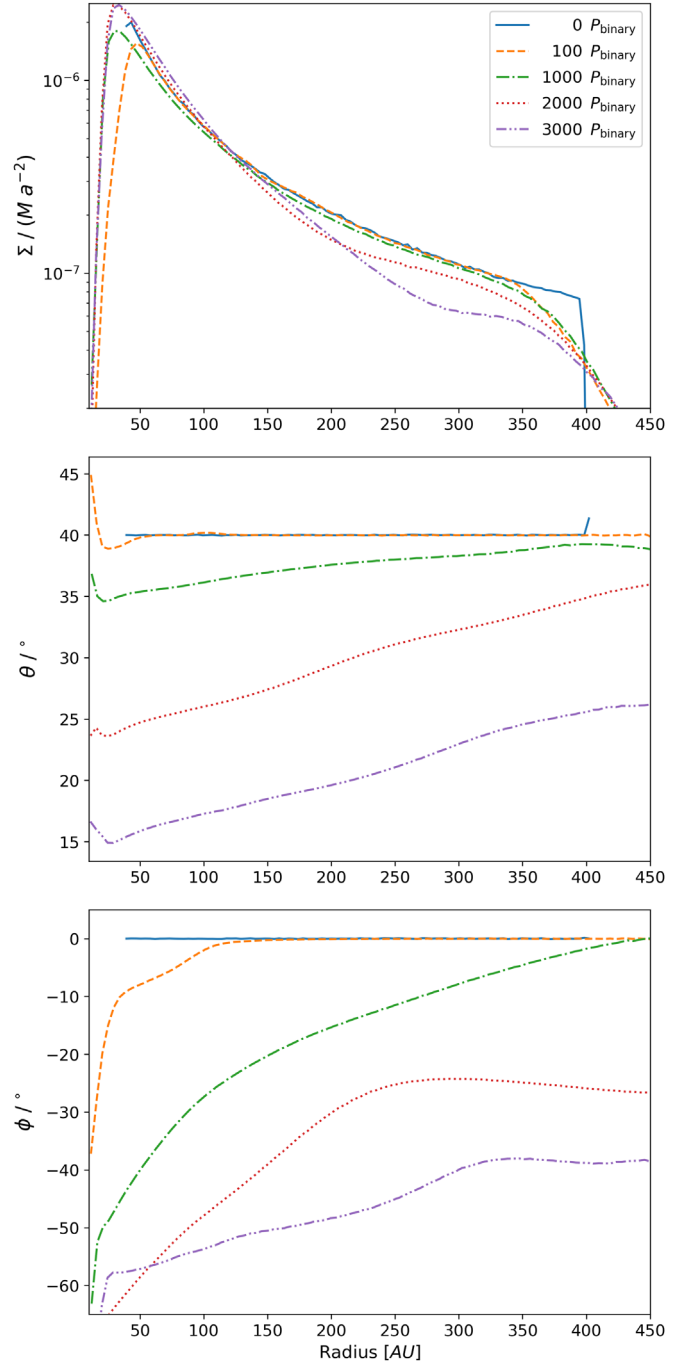


Figure 3. Result of the SPH simulation. Upper panel: radial profile of the surface density of the disk. M and a are the total mass and separation of the AB-C binary in code units, respectively. Middle panel: radial profile of the binary-disk misalignment. Lower panel: radial profile of the longitude of the ascending node of the disk, measured from the binary’s orbital plane.

A disk with a lower aspect ratio or a higher α value, such that it falls into the viscous regime ($h/r < \alpha$), may break due to the binary’s torque (Nixon et al. 2013). However, observations have suggested lower α values than our adaption here (e.g., $\alpha \lesssim 10^{-3}$, Flaherty et al. 2017). A lower viscosity leads to a larger binary truncation radius (Artymowicz & Lubow 1994), and a longer global precession timescale (Equation (D4)). Therefore we expect even less warping (and no break) in the GW Ori disk than in our simulation.

6. Conclusions

We present the ALMA 1.3 mm dust continuum observation and $^{12}\text{CO } J = 2 - 1$ emission of the circumtriple disk around GW Ori. Our main conclusions are the following:

1. For the first time, we identify three dust rings in the GW Ori disk at ~ 46 , 188, and 338 au, with their estimated dust mass being ~ 74 , 168, and $245 M_{\oplus}$, respectively. The three dust rings have enough solids to make many cores of giant planets ($\sim 10 M_{\oplus}$; Pollack et al. 1996).
2. We built three models under various assumptions to fit the dust continuum observations using MCMC fitting. Our results (Table 1) suggest that the inner ring has an eccentricity of ~ 0.2 , and the three rings have statistically different on-sky projected inclinations. The inner, middle, and outer rings are likely misaligned by ~ 11 , 35, and 40 degrees to the orbital plane of the GW Ori AB-C binary system, respectively.
3. A twisted pattern is identified in the first-moment map, suggesting the presence of a warp in the disk, consistent with what we have found in the dust continuum emission.
4. Using analytical analysis and hydrodynamic simulations, we find that the torque from the GW Ori triple stars alone cannot explain the observed large misalignment between the inner and middle dust rings. The disk would not break due to the torque, and a continuous disk is unlikely to show the observed large misalignment. Therefore, this hints at some other mechanism that breaks the disk and prevents radial communication of bending waves between the inner and middle rings.

There are still open questions associated with the system. For example, are there any companions in the disk? Dust rings and gaps have been shown to be common in protoplanetary disks (Andrews et al. 2018; Huang et al. 2018; Long et al. 2018; van der Marel et al. 2019), and one of the most exciting hypotheses is that they are produced by embedded companions ranging from stellar-mass all the way to super-Earths (Artymowicz & Lubow 1994; Dong et al. 2015; Zhang et al. 2018). Specifically, a companion may be opening the gap between the inner and middle rings and breaking the disk there. Companions at hundreds of astronomical units from their host stars have been found before (e.g., HD 106906 b; Bailey et al. 2014). But how they form, i.e., forming in situ or at closer distances, or followed by scattering or migration to the outer regions, is unclear. If GW Ori's dust rings are in the process of forming companions, there will be circumtriple companions, which have not been found before (excluding quadruple systems; Busetti et al. 2018). The system will offer direct clues on the formation of distant companions.

We thank Sean Andrews, Myriam Benisty, John Carpenter, Ian Czekala, Sheng-Yuan Liu, Feng Long, Diego Muñoz, Rebecca Nealon, Henry Ngo, Laura Pérez, John Zanazzi, and Zhaohuan Zhu for discussions. We also thank the anonymous referee for constructive suggestions that largely improved the quality of the paper. J.B. thanks Belaid Moa for help on the numerical implementation. This paper makes use of the

following ALMA data: ADS/JAO.ALMA#2017.1.00286.S. ALMA is a partnership of ESO (representing its member states), NSF (USA) and NINS (Japan), together with NRC (Canada), MOST and ASIAA (Taiwan), and KASI (Republic of Korea), in cooperation with the Republic of Chile. The Joint ALMA Observatory is operated by ESO, auI/NRAO, and NAOJ. The National Radio Astronomy Observatory is a facility of the National Science Foundation operated under cooperative agreement by Associated Universities, Inc. Numerical calculations are performed on the clusters provided by ComputeCanada. This work is in part supported by JSPS KAKENHI grant Nos. 19K03932, 18H05441, and 17H01103 and NAOJ ALMA Scientific Research grant No. 2016-02A. Financial support is provided by the Natural Sciences and Engineering Research Council of Canada through a Discovery Grant awarded to R.D. N.v.d.M. acknowledges support from the Banting Postdoctoral Fellowships program, administered by the Government of Canada. R.G.M. acknowledges support from NASA through grant NNX17AB96G. H.B.L. is supported by the Ministry of Science and Technology (MoST) of Taiwan (grant Nos. 108-2112-M-001-002-MY3). Y.H. is supported by the Jet Propulsion Laboratory, California Institute of Technology, under a contract with the National Aeronautics and Space Administration. K.T. is supported by JSPS KAKENHI 16H05998 and 18H05440, and NAOJ ALMA Scientific Research Grant 2017-05A.

Appendix A ALMA $^{12}\text{CO } J = 2 - 1$ Zeroth-moment Map

Figure A1 shows the ALMA zeroth-moment map of $^{12}\text{CO } J = 2 - 1$ emission. The spiral-like structure at $\sim 0''.75$ to the northwest is likely due to cloud contamination, as reported by previous studies (Czekala et al. 2017; Fang et al. 2017).

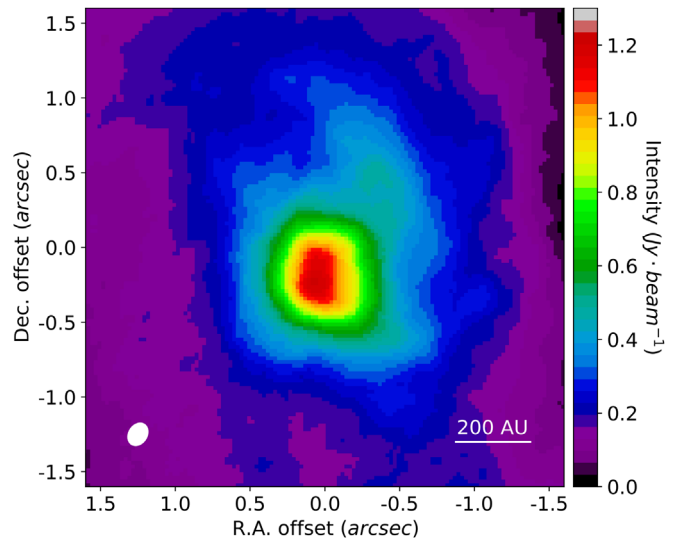


Figure A1. ALMA zeroth-moment map of $^{12}\text{CO } J = 2 - 1$ emission.

Appendix B
A Larger View of Figure 1(a)

Figure B1 shows a larger view of Figure 1(a).

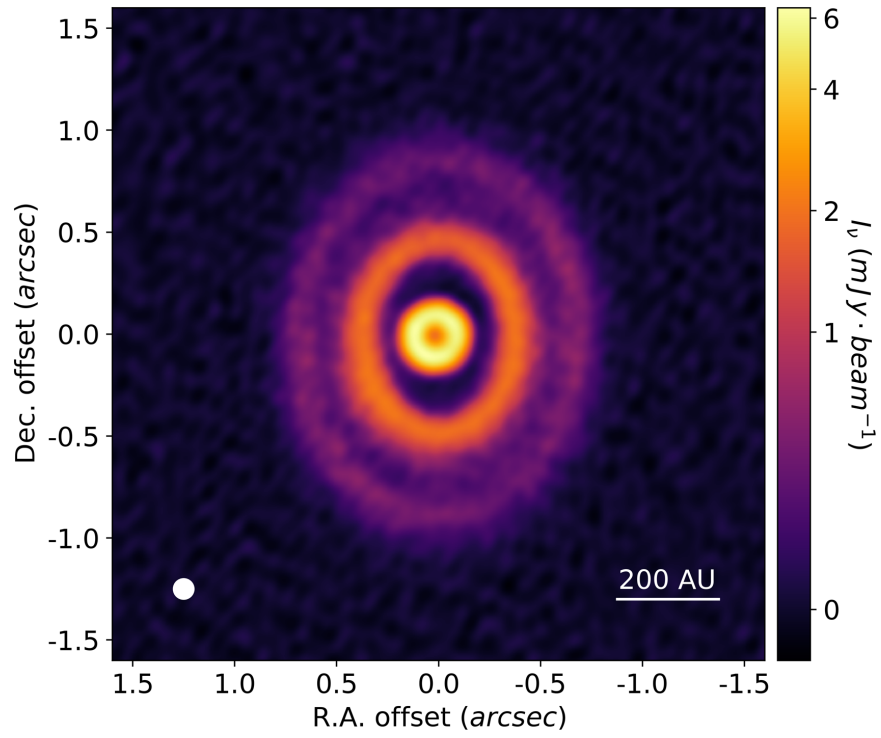


Figure B1. Larger view of Figure 1(a).

Appendix C

The UV-plot and Posterior Distribution of Dust Modeling

Figure C1 shows the uv -plot and posterior distribution of Model 3.

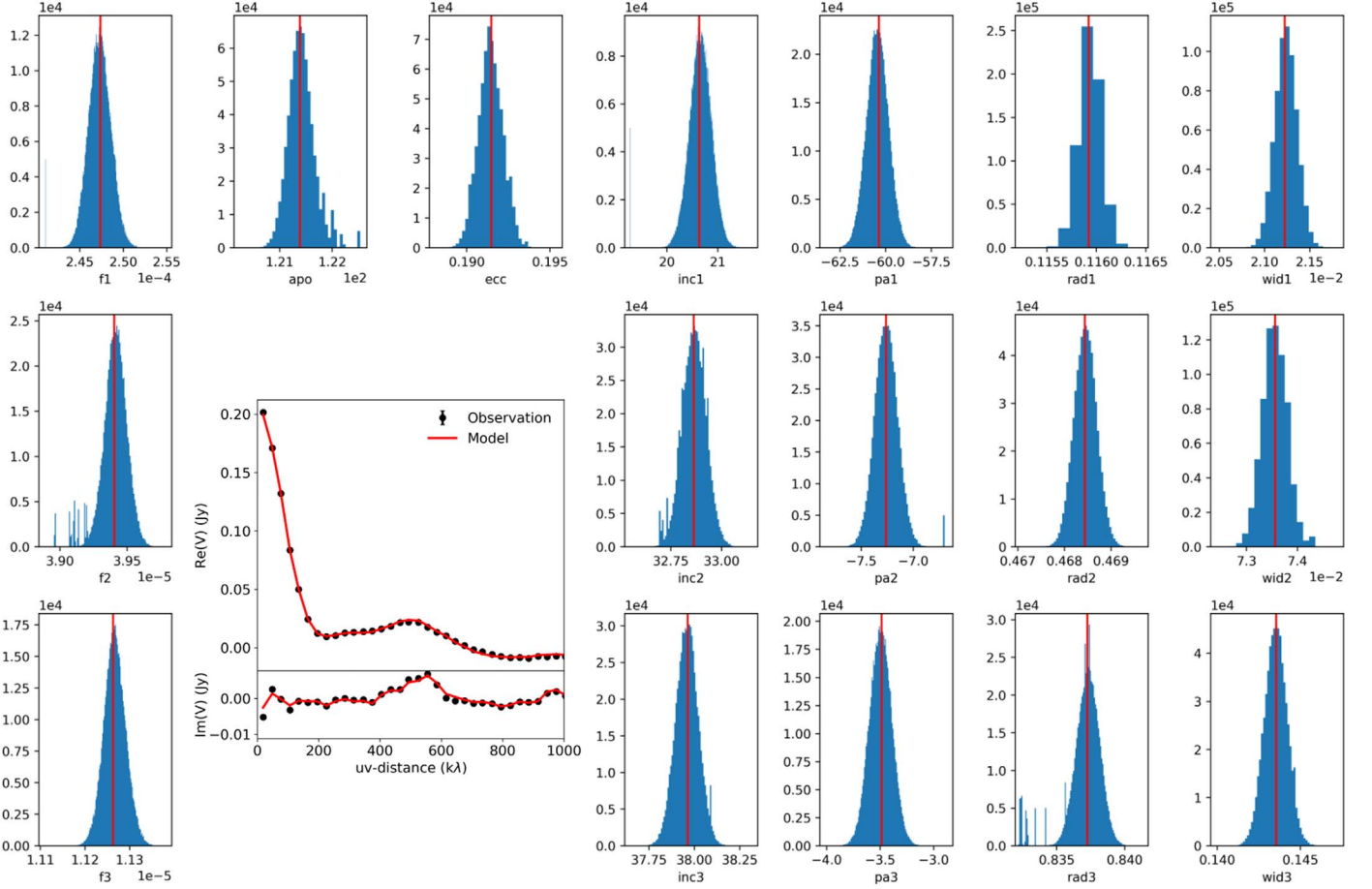


Figure C1. Quality of MCMC parameter search for Model 3. The uv -visibility panel shows the uv -plot of both the ALMA observation and its best-fit model, with the upper panel for the real part of visibility and the lower panel for the imaginary part. The surrounding panels show the histograms of chains in the MCMC fitting. The best-fit value is taken from the fiftieth percentile of the distribution (vertical red line), and the negative and positive uncertainties are taken from sixteenth and eighty-fourth percentile, respectively. The seven columns are for the peak surface brightness, apoapsis angle (inner ring only), eccentricity (inner ring only), inclination, position angle, radius, and width, from left to right. The three rows (top-down) are for the inner, middle, and outer rings. The units of parameters in the histograms are the same as those in Table 1(c).

Appendix D

Equations for the Timescale Analysis

D.1. Radial Communication Timescale

For a disk around a binary system of separation a_b , its radial communication timescale t_c can be estimated by Lubow & Martin (2018)

$$t_c \approx \frac{8}{5\Omega_b(h/r)_{\text{out}}} \left(\frac{r_{\text{out}}}{a_b} \right)^{3/2}, \quad (\text{D1})$$

where r_{out} is the outer radius within which the disk is in good radial communication, and $(h/r)_{\text{out}}$ is the aspect ratio at r_{out} , calculated based on the estimated temperature in the disk (Equation (2)). The radial communication timescale of the entire disk (i.e., $r_{\text{out}} = 1300$ au) is estimated to be ~ 0.06 Myr.

D.2. Nodal Precession Timescale

If there is no radial communication in the disk, each part of the disk shall undergo differential precession with its local precession angular frequency $\omega_{n,\text{local}}$ given by Smallwood et al. (2019)

$$\omega_{n,\text{local}} = k \left(\frac{a_b}{r} \right)^{7/2} \Omega_b, \quad (\text{D2})$$

where

$$k = \frac{3}{4} \sqrt{1 + 3e_b^2 - 4e_b^4} \frac{M_1 M_2}{(M_1 + M_2)^2} \quad (\text{D3})$$

is a constant depending on the eccentricity of binary's orbit e_b , and the primary and secondary mass of the binary M_1 and M_2 . However, for a protoplanetary disk in the bending-wave regime, where radial communication is active and prompt, the disk parts

at different radii shall undergo global precession with the angular frequency $\omega_{n,\text{global}}$ given by Smallwood et al. (2019)

$$\omega_{n,\text{global}} = k \left\langle \left(\frac{a_b}{r} \right)^{7/2} \right\rangle \Omega_b, \quad (\text{D4})$$

and

$$\left\langle \left(\frac{a_b}{r} \right)^{7/2} \right\rangle = \frac{\int_{r_{\text{in}}}^{r_{\text{out}}} \Sigma r^3 \Omega (a_b/r)^{7/2} dr}{\int_{r_{\text{in}}}^{r_{\text{out}}} \Sigma r^3 \Omega dr} \quad (\text{D5})$$

is the angular momentum weighted averaging term, in which $\Omega(r)$ is the angular frequency at a given radius r , $\Sigma(r)$ is the disk surface density with a radial dependence of $r^{-3/2}$, and r_{in} and r_{out} are inner and outer radii of the disk. Assuming $r_{\text{in}} = 32$ au and $r_{\text{out}} = 1300$ au, we take $t_{n,\text{global}} = 2\pi/\omega_{n,\text{global}}$ and estimate the global precession timescale of the entire GW Ori disk to be ~ 0.83 Myr.

D.3. Alignment Timescale

The alignment timescale t_a is given by Lubow & Martin (2018) and Bate et al. (2000)

$$t_a = \frac{(h/r)^2 \Omega_b}{\alpha \omega_n^2}, \quad (\text{D6})$$

where $\alpha = 0.01$, h/r is defined in Equation (6), and the angular frequency of global precession (Equation (D4)) is used for ω_n .

ORCID iDs

Jiaqing Bi  <https://orcid.org/0000-0002-0605-4961>
 Nienke van der Marel  <https://orcid.org/0000-0003-2458-9756>
 Ruobing Dong (董若冰)  <https://orcid.org/0000-0001-9290-7846>
 Rebecca G. Martin  <https://orcid.org/0000-0003-2401-7168>
 Jun Hashimoto  <https://orcid.org/0000-0002-3053-3575>
 Hideko Nomura  <https://orcid.org/0000-0002-7058-7682>
 Michihiro Takami  <https://orcid.org/0000-0001-9248-7546>
 Mihoko Konishi  <https://orcid.org/0000-0003-0114-0542>
 Munetake Momose  <https://orcid.org/0000-0002-3001-0897>
 Kazuhiro D. Kanagawa  <https://orcid.org/0000-0001-7235-2417>
 Akimasa Kataoka  <https://orcid.org/0000-0003-4562-4119>
 Tomohiro Ono  <https://orcid.org/0000-0001-8524-6939>
 Michael L. Sitko  <https://orcid.org/0000-0003-1799-1755>
 Sanemichi Z. Takahashi  <https://orcid.org/0000-0003-3038-364X>
 Kengo Tomida  <https://orcid.org/0000-0001-8105-8113>
 Takashi Tsukagoshi  <https://orcid.org/0000-0002-6034-2892>

References

- Andrews, S. M., Huang, J., Pérez, L. M., et al. 2018, *ApJL*, 869, L41
 Artymowicz, P., & Lubow, S. H. 1994, *ApJ*, 421, 651
 Bailey, V., Meshkat, T., Reiter, M., et al. 2014, *ApJL*, 780, L4
 Bate, M. R. 2012, *MNRAS*, 419, 3115
 Bate, M. R. 2018, *MNRAS*, 475, 5618
 Bate, M. R., Bonnell, I. A., Clarke, C. J., et al. 2000, *MNRAS*, 317, 773
 Beckwith, S. V. W., Sargent, A. I., Chini, R. S., & Guesten, R. 1990, *AJ*, 99, 924
 Benisty, M., Juhász, A., Facchini, S., et al. 2018, *A&A*, 619, A171
 Berger, J. P., Monnier, J. D., Millan-Gabet, R., et al. 2011, *A&A*, 529, L1
 Bonnell, I., & Bastien, P. 1992, *ApJ*, 401, 654
 Bruderer, S. 2013, *A&A*, 559, A46
 Busetti, F., Beust, H., & Harley, C. 2018, *A&A*, 619, A91
 Calvet, N., Muzerolle, J., Briceño, C., et al. 2004, *AJ*, 128, 1294
 Casassus, S., Marino, S., Pérez, S., et al. 2015, *ApJ*, 811, 92
 Czekala, I., Andrews, S. M., Torres, G., et al. 2017, *ApJ*, 851, 132
 Dong, R., Liu, S.-y., Eisner, J., et al. 2018a, *ApJ*, 860, 124
 Dong, R., Najita, J. R., & Brittain, S. 2018b, *ApJ*, 862, 103
 Dong, R., Zhu, Z., & Whitney, B. 2015, *ApJ*, 809, 93
 Facchini, S., Juhász, A., & Lodato, G. 2018, *MNRAS*, 473, 4459
 Fang, M., Sicilia-Aguilar, A., Roccatagliata, V., et al. 2014, *A&A*, 570, A118
 Fang, M., Sicilia-Aguilar, A., Wilner, D., et al. 2017, *A&A*, 603, A132
 Fekel, F. C. J. 1981, *ApJ*, 246, 879
 Flaherty, K. M., Hughes, A. M., Rose, S., et al. 2017, AAS Meeting, 229, 327.07
 Foreman-Mackey, D., Hogg, D. W., Lang, D., & Goodman, J. 2013, *PASP*, 125, 306
 Gaia Collaboration, Brown, A. G. A., Vallenari, A., et al. 2018, *A&A*, 616, A1
 Hildebrand, R. H. 1983, *QJRAS*, 24, 267
 Huang, J., Andrews, S. M., Dullemond, C. P., et al. 2018, *ApJL*, 869, L42
 Huang, J., Andrews, S. M., Dullemond, C. P., et al. 2020, *ApJ*, 891, 48
 Kraus, S., Kreplin, A., Young, A. K., et al. 2020, arXiv:2004.01204
 Lodato, G., & Price, D. J. 2010, *MNRAS*, 405, 1212
 Long, F., Pinilla, P., Herczeg, G. J., et al. 2018, *ApJ*, 869, 17
 Lubow, S. H. 1991, *ApJ*, 381, 259
 Lubow, S. H., & Martin, R. G. 2018, *MNRAS*, 473, 3733
 Marino, S., Perez, S., & Casassus, S. 2015, *ApJL*, 798, L44
 Martin, R. G., & Lubow, S. H. 2017, *ApJL*, 835, L28
 Martin, R. G., & Lubow, S. H. 2019, *MNRAS*, 490, 1332
 Mathieu, R. D., Adams, F. C., & Latham, D. W. 1991, *AJ*, 101, 2184
 McMullin, J. P., Waters, B., Schiebel, D., Young, W., & Golap, K. 2007, in ASP Conf. Ser. 376, *CASA Architecture and Applications*, ed. R. A. Shaw, F. Hill, & D. J. Bell (San Francisco, CA: ASP), 127
 Nixon, C., King, A., & Price, D. 2013, *MNRAS*, 434, 1946
 Nixon, C. J., King, A. R., & Pringle, J. E. 2011, *MNRAS*, 417, L66
 Papaloizou, J. C. B., Nelson, R. P., & Masset, F. 2001, *A&A*, 366, 263
 Pérez, L. M., Benisty, M., Andrews, S. M., et al. 2018, *ApJL*, 869, L50
 Pollack, J. B., Hubickyj, O., Bodenheimer, P., et al. 1996, *Icar*, 124, 62
 Price, D. J., & Federrath, C. 2010, *MNRAS*, 406, 1659
 Price, D. J., Wurster, J., Tricco, T. S., et al. 2018, *PASA*, 35, e031
 Rosenfeld, K. A., Chiang, E., & Andrews, S. M. 2014, *ApJ*, 782, 62
 Shakura, N. I., & Sunyaev, R. A. 1973, *A&A*, 500, 33
 Smallwood, J. L., Lubow, S. H., Franchini, A., & Martin, R. G. 2019, *MNRAS*, 486, 2919
 Tazzari, M., Beaujean, F., & Testi, L. 2018, *MNRAS*, 476, 4527
 van der Marel, N., Dong, R., di Francesco, J., Williams, J. P., & Tobin, J. 2019, *ApJ*, 872, 112
 Walsh, C., Daley, C., Facchini, S., & Juhász, A. 2017, *A&A*, 607, A114
 Zanazzi, J. J., & Lai, D. 2018, *MNRAS*, 473, 603
 Zhang, S., Zhu, Z., Huang, J., et al. 2018, *ApJL*, 869, L47